Advanced Composite Materials
Publication details, including instructions for authors and subscription information:
http://www.tandfonline.com/loi/tacm20

Fiber-optic-based life-cycle monitoring of through-thickness strain in thick CFRP pipes

Kazunori Takagaki[a], Shu Minakuchi[a] & Nobuo Takeda[a]
[a] Department of Advanced Energy, Graduate School of Frontier Sciences, The University of Tokyo, 5-1-5 Kashiwanoha, Kashiwa, Chiba, 277-8561, Japan.
Published online: 09 Oct 2013.

To cite this article: Kazunori Takagaki, Shu Minakuchi & Nobuo Takeda (2014) Fiber-optic-based life-cycle monitoring of through-thickness strain in thick CFRP pipes, Advanced Composite Materials, 23:3, 195-209, DOI: 10.1080/09243046.2013.844901

To link to this article: http://dx.doi.org/10.1080/09243046.2013.844901

Advanced Composite Materials, 2014
Vol. 23, No. 3, 195–209, http://dx.doi.org/10.1080/09243046.2013.844901

Fiber-optic-based life-cycle monitoring of through-thickness strain in thick CFRP pipes

Kazunori Takagaki*, Shu Minakuchi and Nobuo Takeda

Department of Advanced Energy, Graduate School of Frontier Sciences, The University of Tokyo, 5-1-5 Kashiwanoha, Kashiwa, Chiba 277-8561, Japan

(*Received 14 May 2013; accepted 2 September 2013*)

CFRP pipes are used in spacecraft to support heavy optical instruments. CFRPs' low coefficients of thermal expansion and high stiffness improve the instrument performance. However, significant through-thickness strain arises in thick CFRP pipes in curing and operation at low temperature, resulting in delamination failure. In this study, we developed a fiber-optic-based life-cycle monitoring system to measure through-thickness strain development. First, we addressed the mechanism of strain development using a theoretical approach and finite element analysis (FEA). We confirmed that geometrical constraint arising from the cylindrical shapes causes significant out-of-plane stress in the through-thickness center, and the stress increases with increased thickness and stiffness. A fiber Bragg grating (FBG) sensor was then embedded at the through-thickness center of a pipe during lay-up. Non-axisymmetric strain change in the FBG sensor was continuously measured using the birefringence effect throughout the life cycle, including curing and simulated operation in a low temperature environment. Through comparison between pipe and plate specimens, it was clearly demonstrated that the system could sensitively capture through-thickness strain development and detect delamination failure in the pipe. In addition, FEA was conducted and the result agreed well with the experiment data, confirming the validity of the experiment results.

Keywords: CFRP pipe; through-thickness strain; FBG sensor; life-cycle monitoring

1. Introduction

Truss structures supporting heavy optical telescopes in spacecraft are required to have a low coefficient of thermal expansion (CTE) below $10^{-6}\,K^{-1}$ in order to achieve high observation accuracy. For this reason, CFRP pipes made of pitch-based graphite fibers are utilized for those components.[1,2] Figure 1 depicts a schematic of a support structure of the SOLAR-B (high-precision solar physics satellite) with an optical telescope. [3] Recently, the thickness and modulus of CFRP pipes have been increased due to the increased size of optical instruments. In thick, high-modulus CFRP pipes, however, significant through-thickness tensile stress arises during curing or operation in a low temperature environment, resulting in delamination failure.[4–6] Figure 2 depicts the distribution of through-thickness stress that developed during cooling in the curing process, calculated by finite-element analysis (FEA). Maximum through-thickness stress arises near the center of the thickness, causing delamination after curing (Figure 3).

*Corresponding author. Email: takagaki@smart.k.u-tokyo.ac.jp

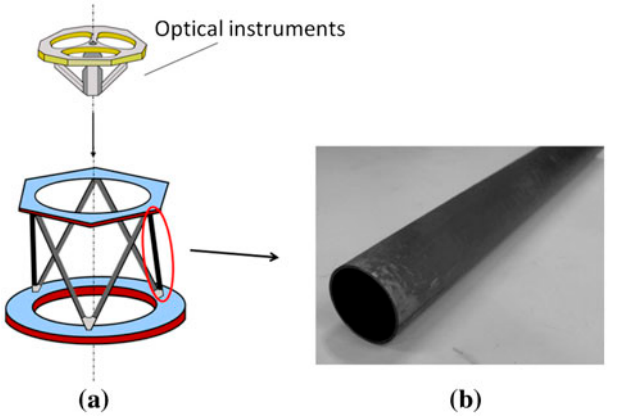

Figure 1. Images of (a) support structure and (b) CFRP pipe.

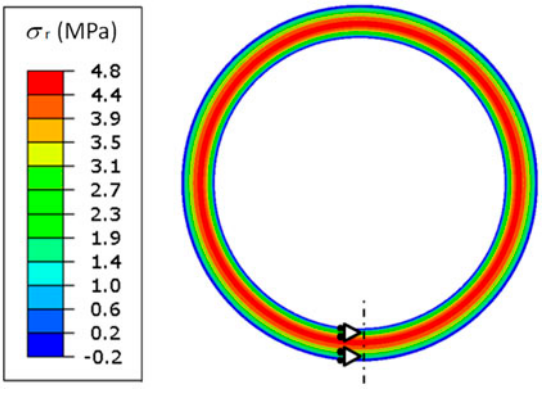

Figure 2. Stress distribution after cooling (carbon/epoxy $[0_2/90_2]_{4S}$; thickness 3.45 mm, inner radius 15 mm, ΔT −105 °C, and 0^o longitudinal direction).

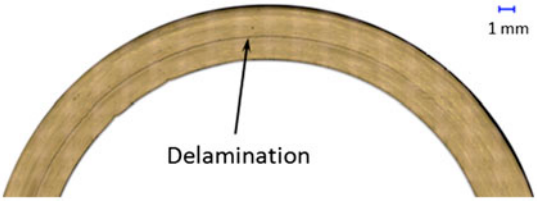

Figure 3. Cross-sectional micrograph of delamination in CFRP pipe after curing.

Although many previous studies focused on strain development in composite pipes,[4–14] no technique for directly measuring the out-of-plane strain resulting in delamination has been developed, and the underlying mechanism of stress/strain development leading to delamination failure has not been sufficiently clarified.

In this study, we develop a fiber-optic-based life-cycle monitoring system [15,16] in order to obtain new insight into the through-thickness strain development and improve

reliability of CFRP pipes. We begin by analyzing through-thickness stress development using FEA and the classical lamination theory. Consequent strain development in CFRP pipes is then continuously measured, using responses of optical fiber sensors embedded during lay-up, throughout the life cycle including the curing process and a low-temperature test. Finally, delamination detection is demonstrated.

2. Through-thickness stress development in thick pipes

2.1. FEA

FEA was conducted using Abaqus 6.11 to calculate thermal stress development in a CFRP pipe. Figure 4(a) illustrates the 2D FEA model, assuming a plane strain state. One-fourth of a pipe was modeled for simplification, and the inner radius was set at 15 mm. In order to simulate a cooling phase, a 105 °C temperature decrease was applied along with constraint on both edges (Figure 4(a)). This model was labeled the 'whole model.' In order to evaluate the effect of geometrical constraint arising from the cylindrical shape, a model with constraint on only one edge was also developed (Figure 4(b)). This model was labeled the 'no-constraint model,' since this is the same as a 1/2 C-shaped open section that has no constraint on the both edges. The ply thickness was set to 0.11 mm based on experiment data; the material properties used in the analysis were taken from published work [17] and are summarized in Table 1.

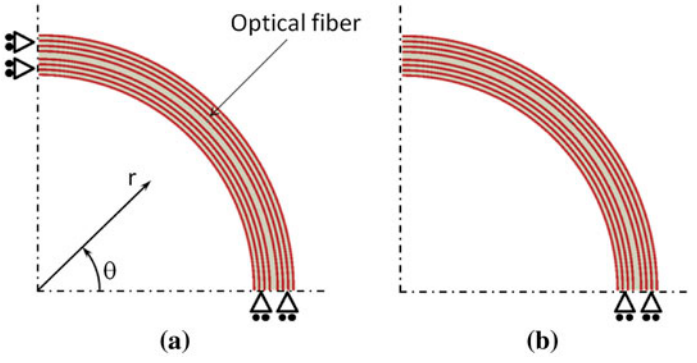

Figure 4. Schematic of the FEA model: (a) whole model and (b) no-constraint model (magnification factor is 25).

Table 1. Material properties used in analysis.

		HYEJ15M65PD-25 unidirectional	Cladding and core	Polyimide coating
Elastic moduli (GPa)	E_{11}	350	73.1	1.5
	E_{22}	5		
	G_{12}	4.2		
	G_{23}	2.0		
Poisson's ratios	ν_{12}	0.33	0.16	0.25
	ν_{23}	0.445		
Thermal expansion coefficients ($\times 10^{-6}$/°C)	α_{11}	−0.3	0.5	15
	α_{22}	40.0		

Figure 5 plots the circumferential (θ direction) and through-thickness (r direction) stress in a $[90_2/0_2]_{4S}$ pipe. In this figure, 0^o is the longitudinal direction, and 90^o is the circumferential direction. Figure 6 plots the maximum through-thickness stresses in $[90_2/0_2]_{nS}$ pipes, where n is set to 1, 2, 4, and 8. In Figure 5, the horizontal axis, R, is the normalized distance in the radial direction:

$$R = \frac{r - r_0}{t} \quad (0 \leqslant R \leqslant 1), \tag{1}$$

where r is the distance from the center of the pipe, r_0 is the internal radius, and t is the thickness. In Figure 6, the horizontal axis, r_0/t, is the ratio of internal radius to

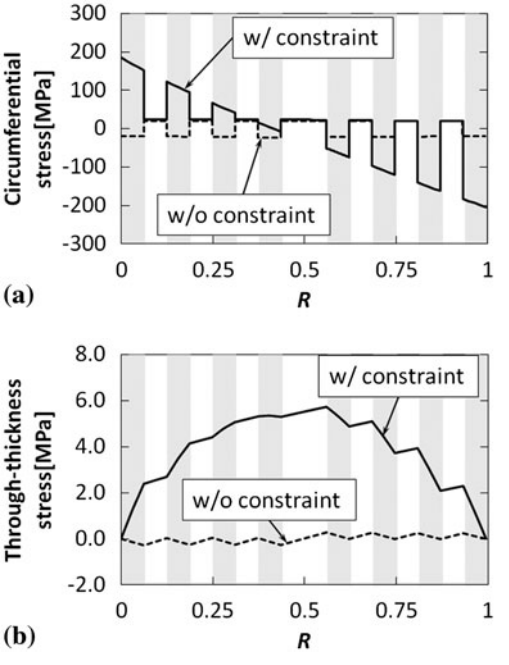

Figure 5. Stress distribution in $[90_2/0_2]_{4S}$ pipe (FEA): (a) circumferential stress and (b) through-thickness stress.

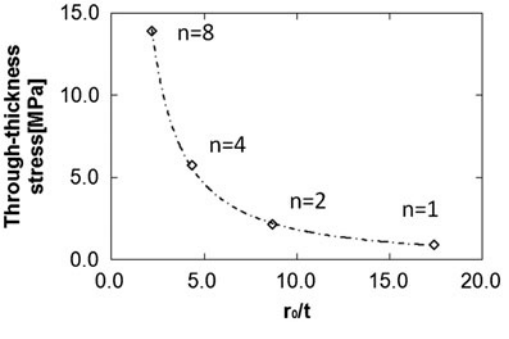

Figure 6. Relationship between r_0/t and maximum through-thickness stress in pipe (FEA).

thickness. Figure 5 indicates that stress development in the pipe is attributed mainly to its geometrical constraint arising from the cylindrical shape because both the circumferential and through-thickness stresses of the whole model with constraint at both edges are much higher than those of the no-constraint model. Additionally, the maximum radial stress increases with increased thickness (Figure 6).

2.2. Theoretical approach

Theoretical calculation was conducted to clarify the underlying mechanism of the through-thickness stress development presented above. The thermal stress in composite pipes has been strictly formulated in previous research,[7] but a simpler approach was used here, in an effort to focus on the main cause of stress development. The equation of equilibrium in the radial direction in a cylindrical coordinate system is given by

$$\frac{\partial \sigma_r}{\partial r} + \frac{\partial \tau_{\theta r}}{r \partial \theta} + \frac{\sigma_r - \sigma_\theta}{r} + \frac{\partial \tau_{zr}}{\partial z} = 0, \tag{2}$$

where σ is the normal stress, τ is the shear stress, r is the radial (e.g. through-thickness) direction, θ is the circumferential direction, and z is the longitudinal direction.[18] Assuming plane strain and axisymmetry, Equation (2) is simplified to

$$\frac{\partial \sigma_r}{\partial r} + \frac{\sigma_r - \sigma_\theta}{r} = 0. \tag{3a}$$

Integrating Equation (3) gives the radial stress at distance r as

$$\sigma_r = \frac{1}{r}\int_{r_0}^{r} \sigma_\theta d\tilde{r} = \frac{1}{r_0/t + R}\int_0^R \sigma_\theta d\tilde{R}, \tag{3b}$$

where r_0 is the internal radius, t is the thickness, and R is the normalized distance defined by Equation (1). Consequently, the radial stress at normalized distance R is determined by the ratio of the internal radius to the thickness, r_0/t, and the circumferential stress distribution σ_θ.

Next, the circumferential stress σ_θ in the pipe was separated into 'stress developed during cooling without constraint on both edges' (developed in the no-constraint model) and 'stress developed by geometrical constraint after cooling' (the difference between stresses developed in the whole model and the no-constraint model). The stress during cooling without constraint is almost identical to the stress developed in a plate with the same stacking sequence. The stress in the 0^o direction is given as

$$\sigma_\theta = \frac{E_1 E_2(\alpha_1 - \alpha_2)}{E_1 + E_2}\Delta T \approx 21 \text{ [MPa]}, \tag{4}$$

where E is the Young's modulus, α is the CTE, ΔT is the temperature change, subscript 1 denotes composite fiber direction, and subscript 2 denotes transverse direction. The calculated value agreed well with the FEA result (21 MPa; Figure 5). Equation (4) indicates that the stress without constraint is determined only by material properties (i.e. Young's modulus and CTE) and temperature change. In contrast, the stress development due to the geometrical constraint arises by correcting the thermally

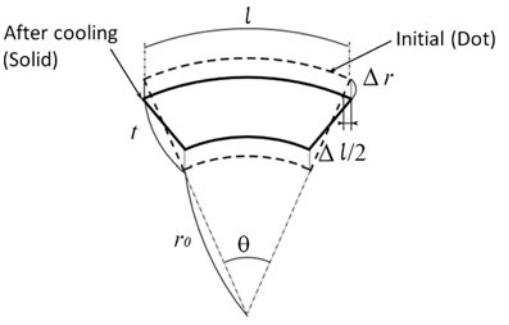

Figure 7. Schematic of spring-in.

distorted part (i.e. spring-in deformation [19,20]) to a cylindrical shape. Figure 7 illustrates a schematic of one part of a pipe, where the dotted line is the shape before cooling, and the solid line is that after cooling. Here, r_0 is the internal radius, t is the thickness, and l is the length of the external layer. In a $[90_2/0_2]_{4S}$ cross-ply laminate, in-plane reinforcing fibers constrain both longitudinal and circumferential deformations, so uniform through-thickness thermal strain,

$$\varepsilon_r = \alpha_r(1 + \nu_{23})\Delta T, \tag{5}$$

was assumed to be induced. Here, α_r is the CTE in the radial direction (α_{22} in Table 1), and ν_{23} is the Poisson ratio. The radial displacement Δr, the circumferential strain change induced by shape correction at the outermost layer ε_θ, and the consequent circumferential stress σ_θ are expressed as follows.

$$\Delta r = \frac{1}{2}\, t \cdot \varepsilon_r = \frac{1}{2}\, t \cdot \alpha_r(1 + \nu_{23})\Delta T \tag{6a}$$

$$\varepsilon_\theta = \frac{\Delta l}{l} = \frac{(r_0 + t + \Delta r)\theta - (r_0 + t)\theta}{(r_0 + t)\theta} = \frac{\Delta r}{r_0 + t} \tag{6b}$$

$$\sigma_\theta \approx E_\theta \varepsilon_\theta = \frac{E_\theta \Delta r}{r_0 + t} = \frac{1}{2} \cdot \frac{E_\theta \alpha_r(1 + \nu)\Delta T}{1 + r_0/t} \approx -199[\mathrm{MPa}] \tag{6c}$$

The calculated value is slightly higher than the FEA result (−180 MPa) mainly due to the assumption of uniform thermal strain. However, Equation (6c) implies that r_0/t representing the geometry of the pipe affects the stress generated by geometrical constraint, in addition to material properties and temperature change.

In summary, Equations (4) and (6c) indicate that the geometrical constraint stress is dominant in thick pipes. Furthermore, the circumferential stress induced by the geometrical constraint increases with increased in-plane Young's modulus E_θ and thickness t (Equation (6c)), resulting in the development of significant radial stress σ_r (Equation (3)). Thus, the theoretical approach clearly demonstrated that the geometrical constraint arising from the cylindrical shape is the main cause of stress development in high-modulus, thick CFRP pipes.

3. Life-cycle monitoring

3.1. Measurement using the birefringence effect of the FBG sensor

Figure 8 presents a schematic for life-cycle monitoring of a composite pipe for spacecraft structures. This study evaluates the through-thickness strain in pipes using responses of fiber Bragg grating (FBG) sensors embedded during lay-up. An FBG sensor has periodic variation in the refractive index along the length of a single-mode optical fiber. When broadband light is launched into the FBG sensor, a narrow spectral component is reflected back, and the reflection spectrum gives the measurement of strain and/or temperature. When non-axisymmetric strain arises at the center of the cross-section of the FBG sensor, the reflection spectrum splits into two peaks, due to the birefringence effect (Figure 9) [21,22]. The difference between the central wavelengths $\Delta\lambda$ of two peaks, λ_p and λ_q, is expressed as

$$\Delta\lambda = |\lambda_q - \lambda_p| = n_0^2(p_{12} - p_{11})\,\lambda_0\frac{|\varepsilon_1 - \varepsilon_2|}{2}, \tag{7}$$

where n_0 is the initial refractive index of the optical fiber core, λ_0 is the center wavelength of the initial reflection spectrum, p_{11} and p_{12} are the photo-elastic constants, and ε_1 and ε_2 are the principal strains at the core in the cross-sectional direction of the FBG sensor. Equation (7) indicates that $\Delta\lambda$ is proportional to the non-axisymmetric strain defined as

$$\varepsilon_d = \frac{|\varepsilon_1 - \varepsilon_2|}{2}, \tag{8}$$

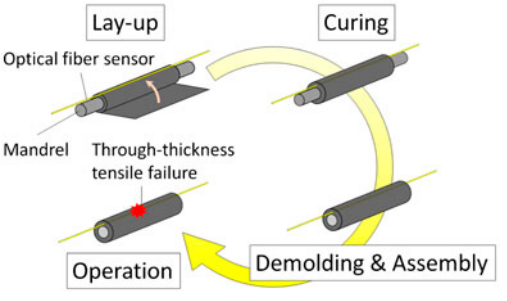

Figure 8. Schematic of life-cycle monitoring of CFRP pipe.

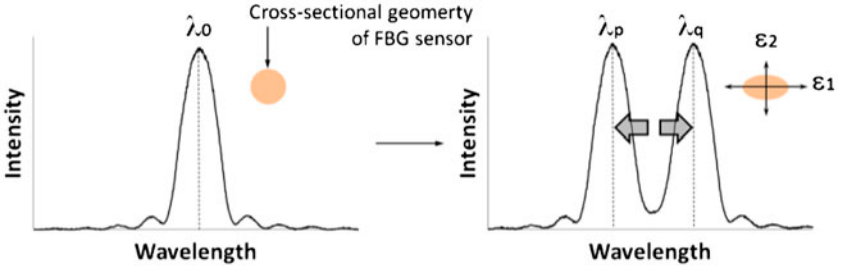

Figure 9. Spectrum change induced by birefringence.

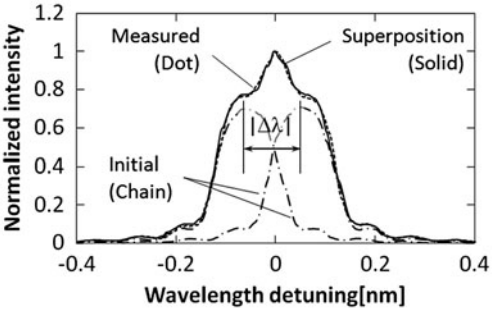

Figure 10. Comparison of measured spectrum and superposition of two initial spectra.

which represents the flattening of the sensor's cross-sectional shape. The response of the FBG sensor can be reproduced by superposing the two initial spectra $\Delta\lambda$ away from one another (Figure 10), so the difference between the circumferential strain and through-thickness strain, $|\varepsilon_\theta - \varepsilon_r|$, can be obtained by calculating $\Delta\lambda$ from the measured FBG spectrum. A Fortran program was used to calculate the difference between the central wavelengths, $\Delta\lambda$, where the sum of squares of the difference between the measured and superposed spectra was minimum. Additionally, the constant in Equation (7)

$$n_0^2(p_{12} - p_{11}) = k \tag{9}$$

was determined to be 0.42 from preliminary monitoring tests using several materials whose properties were known.

It is important to note that strain transfer between the host material and an embedded optical fiber sensor is not perfect (i.e. strains in material and an optical fiber are different) in the cross-sectional direction, because the optical fiber sensor is thin (diameter: 150 μm) and its material (i.e. fused silica glass) is stiff. The internal strain state of the host material, however, can be directly evaluated using the optical fiber sensor, since the strain at the center of the sensor is proportional to the strain of the host material in the vicinity of the sensor.[23] Furthermore, the radial strain ε_r is dominant near the through-thickness center where the circumferential strain change is small (Figure 5), so the non-axisymmetric strain ε_d is a good indicator of radial strain change near the through-thickness center. Thus, this study embeds FBG sensors near the through-thickness center and measures the non-axisymmetric strain ε_d.

3.2. Process monitoring

3.2.1. Materials and methods

Two experiments were conducted in order to validate the proposed monitoring technique during curing. Figure 11 presents a schematic of the specimen. The material is pitch-based carbon/epoxy prepreg HYEJ15M65PD-25 (Mitsubishi Plastics, Inc.). Two stacking sequences were used: $[0_2/90_2]_{4S}$ (32 plies and 3.5 mm-thick after curing; '32-ply specimen') and $[0_2/90_2]_{6S}$ (48 plies and 5.2 mm-thick after curing; '48-ply specimen'). During lay-up, FBG sensors (Fujikura Ltd., polyimide-coating diameter: 150 μm, and grating length: 10 mm) were embedded between the 19th and 20th plies (32-ply specimen), and the 27th and 28th plies (48-ply specimen) parallel to the local

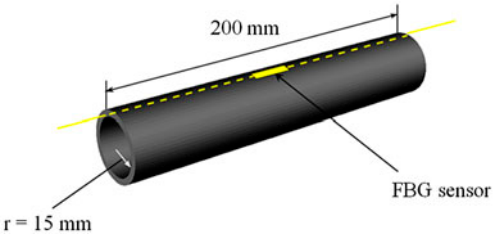

Figure 11. Schematic of specimen.

carbon fiber direction near the through-thickness center. The optical fibers were illuminated by an amplified spontaneous emission (ASE) light source (AQ2141, Ando Electric Co., Ltd.), and the reflection spectra from the FBGs were measured using an optical spectrum analyzer (AQ6317, Ando Electric Co., Ltd.). Additionally, temperature was measured using thermocouples embedded near the sensors.

Tightly laid-up prepreg became loose during vacuuming and compaction when all the plies were cured at one time; consequently, large wrinkles accompanying carbon fiber failure arose after curing. Hence, curing was conducted separately: 13, 10, and 9 plies for the 32-ply specimen; and 13, 8, 10, 8, and 9 plies for the 48-ply specimen. A 15 mm-outer-radius aluminum mandrel coated with a release agent (Chemlease AF-7, Chemlease Japan Co., Ltd.) was utilized for the first cure (13 plies). After the second curing, however, prepreg was directly laminated onto the cured specimen without a mandrel. Thus, contact between the specimen and the mandrel did not affect the FBG response. After lay-up, the specimen was pressured by a thermal shrinkage tube, vacuum-bagged, and then cured in an autoclave under a gage pressure of 0.5 MPa. The cure cycle was 2 °C/min heating, 125 °C holding for 2 h, and 2 °C/min cooling. Since each layer was made of one sheet of the prepreg, carbon fibers were discontinuous at the joints of the 90° fiber layers. However, preliminary FEA confirmed that the effect of the discontinuities on the FBG response is small; and the effect was further reduced by embedding FBG sensors away from the equally distributed discontinuities.

A test using a 32-ply 'plate' specimen ($[0_2/90_2]_{4S}$, 200 mm × 200 mm) was also conducted. The response of an FBG embedded between the 19th and 20th plies (i.e. the same position as in the pipe specimen) was measured in order to evaluate the effect of geometrical constraint, which is considered the main cause of through-thickness stress development in thick CFRP pipes.

3.2.2. *Experiment results*

Figure 12 indicates the non-axisymmetric strain and temperature change of the second and third cures of the 32-ply pipe specimen. Figure 13 compares the non-axisymmetric strain responses of the 32-ply pipe and plate specimens. In both tests of the pipe specimen (Figure 12), the non-axisymmetric strain significantly increased during the cooling phase after 200 min, due mainly to the difference between the radial and circumferential CTEs of CFRP.[16,21] It is interesting to note that the strain also increased before 200 min in the second cure (Figure 12(a)). The strain variation during 0–100 min was due to measurement and Fortran program calculation error. However, the strain became stable at 30 με during retention temperature for curing (100–200 min). The non-axisymmetric strain increase indicates that the FBG sensor measured strain development by

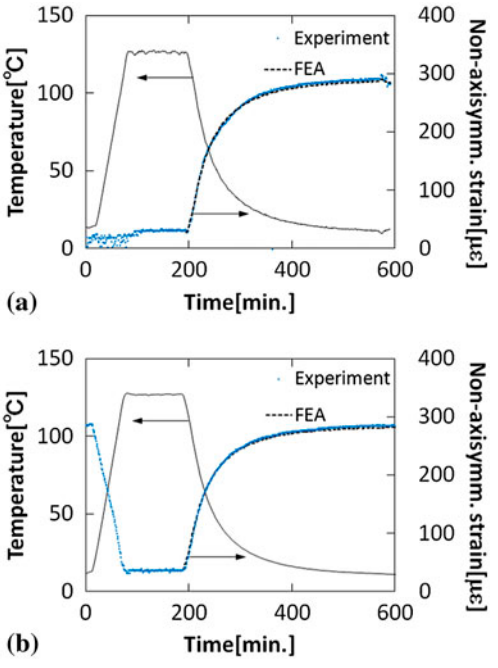

Figure 12. Non-axisymmetric strain change during curing (32-ply specimen): (a) second cure, 23 ply and (b) third cure, 32 ply.

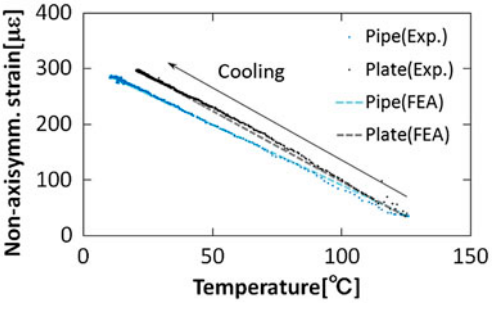

Figure 13. Non-axisymmetric strain change during cure (32-ply pipe and plate).

resin chemical cure shrinkage. The strain increase and its magnitude were consistent in several similar tests, affirming the above speculation. In the subsequent third cure (Figure 12(b)), the non-axisymmetric strain decreased up to the irreversible cure strain of 30 με with relaxation of the thermal residual strain during heating, and then increased again during cooling. Figure 13 indicates the non-axisymmetric strain change in the pipe and plate specimens during cooling. The difference between the pipe and plate is attributed to the radial strain difference since the circumferential strain is negligible near the through-thickness center, confirming that the FBG sensor embedded in the pipe specimen could sensitively capture the radial strain development induced by the geometrical constraint.

Figure 14 presents the results of the third and fourth cures of the 48-ply specimen. As with the 32-ply specimen, the FBG sensor measured the non-axisymmetric strain increase induced by cure and thermal shrinkage. In Figure 14(b), however, the non-axisymmetric strain change was discontinuous near 300 min. This discontinuous strain change was attributed to through-thickness failure because delamination was observed in the cross-section after the fourth cure of the 48 ply specimen (Figure 15). Thus, the FBG sensor detected delamination in the pipe in real time, in addition to the radial strain measurement. The fifth cure process was not conducted, due to the delamination failure in the fourth cure.

Figures 12–14 plot the non-axisymmetric strain changes calculated by FEA simulating cooling phase. In the FEA, temperature decrease was applied on a plane strain model having pipe shape. The inner radius was set at 15 mm and thickness was determined based on experiment data. The results plotted in Figures 12–14 are summations of the strain measured before cooling and the strains obtained by FEA. The strain induced by resin curing was not calculated here since a preliminary study indicated that non-axisymmetric strain induced by cure shrinkage cannot be accurately calculated without considering the viscoelastic behavior in a rubbery state that could not be obtained in this study. The FEA results agreed well with the experiment results, except after the delamination failure (Figure 14(b)), confirming the validity of the measurement. One cause of the mismatch between the experiment and the FEA results in Figure 14(b) is that the delamination failure in the FEA was modeled based on cross-sectional observation after cooling. Hence, the developed model might differ from the actual specimen during cooling, underestimating the strain increase by delamination.

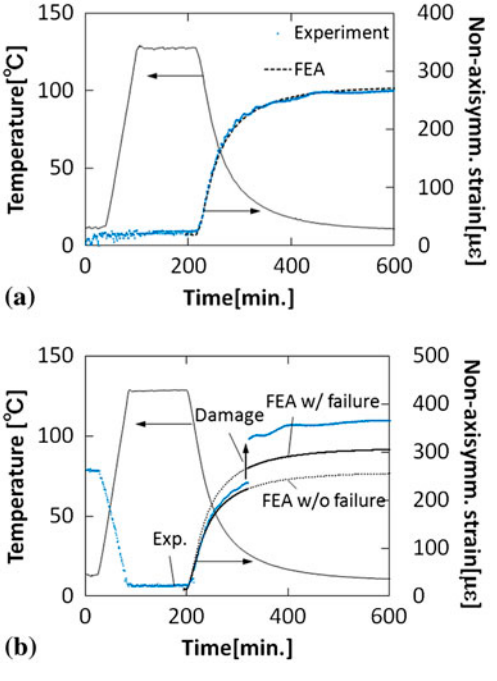

Figure 14. Non-axisymmetric strain change during cure (48-ply specimen): (a) third cure, 31 ply and (b) fourth cure, 39 ply.

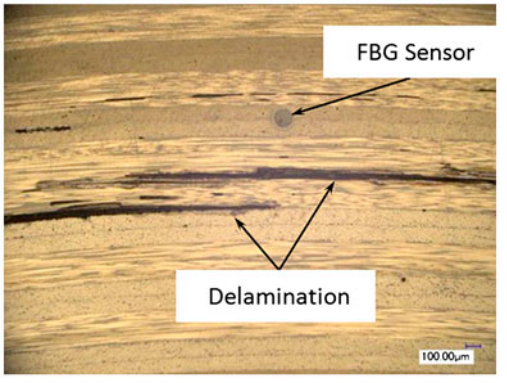

Figure 15. Cross-section of 48-ply specimen after curing.

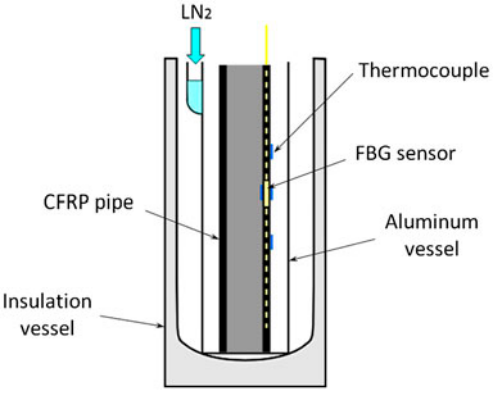

Figure 16. Schematic of low-temperature test setup.

Nonetheless, the experiment trend that the non-axisymmetric strain increased after delamination agreed with the FEA result, successfully demonstrating fiber-optic-based radial strain monitoring and damage detection throughout curing.

3.3. Strain and damage monitoring in the low-temperature test

3.3.1. Materials and methods

Next, a low-temperature test simulating the temperature environment in space was conducted with the 32-ply pipe ($[0_2/90_2]_{4S}$) made in the previous section. As illustrated in Figure 16, an aluminum vessel was installed in an insulation vessel, and the specimen was cooled from room temperature to −100 °C using liquid nitrogen (LN_2), while continuously measuring the FBG response. LN_2 was placed in a holder attached to the upper part of the aluminum vessel in order to reduce temperature distribution in the longitudinal direction. In addition, four thermocouples were attached at the front and back surfaces of the point where the FBG sensor was embedded and at the front surface of 35 mm upper and lower sides from the FBG point. Cooling was performed by adjusting the amount of LN_2 in order to keep the measured temperature difference within 2 °C.

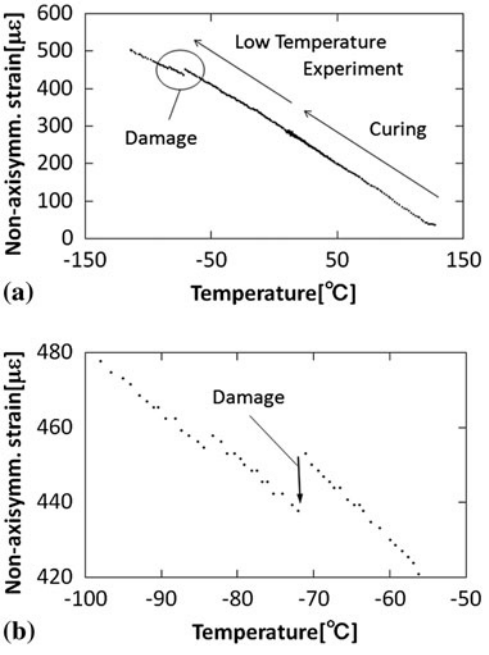

Figure 17. Non-axisymmetric strain change: (a) life-cycle change and (b) from −50 °C to −100 °C.

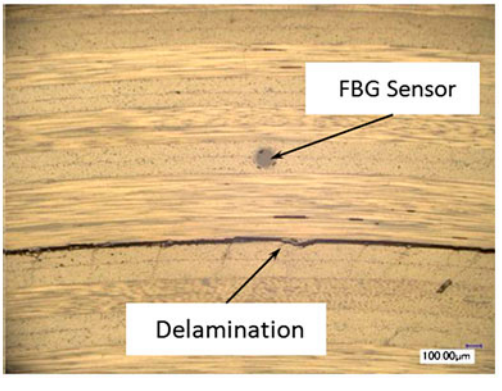

Figure 18. Cross-section of 32-ply specimen after low-temperature test.

3.3.2. *Experiment results*

Figure 17(a) plots the non-axisymmetric strain change during the simulated life cycle (i.e. cure and operation in low temperature), and Figure 17(b) depicts a magnified plot from −50 °C to −100 °C. From room temperature to −70 °C, the FBG sensor monitored the radial strain development, as during the curing process. However, there was a discontinuous change of the non-axisymmetric strain near −70 °C. Since delamination was observed in the cross-section after the low-temperature test (Figure 18), this

discontinuous change was attributed to delamination failure, as in the cure test of the 48-ply specimen. Thus, radial strain/damage monitoring was successfully demonstrated in a low temperature environment.

4. Conclusions

This study began with an analysis of the through-thickness stress development in composite pipes, clarifying the effects of pipe geometry and material properties. A life-cycle monitoring system for thick CFRP pipes was then developed using FBG sensors. It was confirmed that the out-of-plane strain in pipes that causes delamination could be continuously measured using embedded FBG sensors throughout the life cycle from curing to a low-temperature test simulating the space temperature environment, and that delamination failure could be detected in real time. Comparison between pipe and plate specimens demonstrated high sensitivity of the system to through-thickness strain induced by geometrical constraint arising from cylindrical shape. In addition, FEA results agreed well with experiment data, confirming the validity of the experiment results.

However, it should be noted that the failure stress of CFRP pipes was significantly less than the transverse strength of CFRP laminates (FEA calculated 6.7 MPa in the fourth cure of the 48-ply specimen and 8.5 MPa in the low-temperature test) and that the effects of multi-axial stress state and resin cure shrinkage [5,6] should be investigated further. An FBG sensor might be an effective tool for investigating chemical cure shrinkage strain, as it measured the strain change during cure (Figures 12 and 14). Furthermore, the result obtained indicated that reduction of through-thickness stress is a key issue in manufacturing much thicker high-modulus CFRP pipes. In future work, we will establish a new methodology for manufacturing delamination-free thick CFRP pipes by combining optimization of the curing process and design with stress/strain evaluation using the FBG sensor measurement developed in this study.

Acknowledgments

The authors acknowledge support from the Ministry of Education, Culture, Sports, Science and Technology of Japan under a Grant-in-Aid for Scientific Research (A) (No. 23246146) and are grateful to Mitsubishi Plastics, Inc., for providing the material.

References

[1] Ozaki T, Naito K, Mikami I, Yamauchi H, Tsuneta S. High precision composite pipes for SOLAR-B optical structures. Acta Astronautica. 2001;48:321–329.
[2] Ozaki T, Ikeda C, Isoda M, Tsuneta S. A new high-thermal-conductivity composite material for high-precision space optics. Proc. SPIE. 1996;2804:22–31.
[3] Suematsu Y, Tsuneta S, Ichimoto K, Simizu T, Otsubo M, Katsukawa Y, Nakagiri M, Noguchi M, Tamura T, Kato Y, Hara H, Kubo M, Mikami I, Saito H, Matsushita T, Kawaguchi N, Nakaoji T, Nagae K, Shimada S, Takeyama N, Yamamuro T. The solar optical telescope of Solar-B (Hinode): the optical telescope assembly. Solar Phys. 2008;249:197–220.
[4] Sekine H, Shin ES. Optimum design of thick-walled multi-layered CFRP pipes to reduce process-induced residual stresses. Appl. Compos. Mater. 1999;6:289–307.
[5] Wisnom MR, Stringer LG, Hayman RJ, Hinton MJ. Curing stresses in thick polymer composite components, Part I: analysis. In: Proc. ICCM12; 1999. Paper number 859.
[6] Stringer LG, Hayman RJ, Hinton MJ, Badcock RA, Wisnom MR. Curing stresses in thick polymer composite components Part II: Management of residual stresses. In: Proc. ICCM12; 1999. Paper number 861.

[7] Jacquemin F, Vautrin A. Analytical calculation of the transient thermoelastic stresses in thick walled composite pipes. J. Compos. Mater. 2004;38:1733–1751.
[8] Kaddour AS, Al-Hassani STS, Hinton MJ. Residual stress assessment in thin angle ply tubes. Appl. Compos. Mater. 2003;10:169–188.
[9] Casari P, Jaquemin F, Davies P. Characterization of residual stresses in wound composite tubes. Compos. Part A. 2006;37:337–343.
[10] Hernández-Moreno H, Collombet F, Douchin B, Choqueuse D, Davies P, González Velázquez JL. Entire life time monitoring of filament wound composite cylinders using Bragg grating sensors: I. Adapted tooling and instrumented specimen. Appl. Compos. Mater. 2009;16:173–182.
[11] Hernández-Moreno H, Collombet F, Douchin B, Choqueuse D, Davies P, González Velázquez JL. Entire life time monitoring of filament wound composite cylinders using Bragg grating sensors: II. Process monitoring. Appl. Compos. Mater. 2009;16:197–209.
[12] Hernández-Moreno H, Collombet F, Douchin B, Choqueuse D, Davies P. Entire life time monitoring of filament wound composite cylinders using Bragg grating sensors: III. In-service external pressure loading. Appl. Compos. Mater. 2009;16:135–147.
[13] Xia M, Takayanagi H, Kemmochi K. Analysis of multi-layered filament-wound composite pipes under internal pressure. Compos. Struct. 2001;53:483–491.
[14] Kobayashi S, Imai T, Wakayama S. Burst strength evaluation of the FW-CFRP hybrid composite pipes considering plastic deformation of the liner. Compos. Part A. 2007;38:1344–1353.
[15] Minakuchi S, Takeda N, Takeda S, Nagao Y, Franceschetti A, Liu X. Life cycle monitoring of large-scale CFRP VARTM structure by fiber-optic-based distributed sensing. Composites Part A. 2011;42:669–676.
[16] Minakuchi S, Umehara T, Takagaki K, Ito Y, Takeda N. Life cycle monitoring and advanced quality assurance of L-shaped composite corner part using embedded fiber-optic sensor. Compos. Part A. 2013;48:153–161.
[17] Arao Y, Koyanagi J, Takeda S, Utsunomiya S, Kawada H. Out-of-plane deformation due to the ply angle misalignment in CRFP laminates (the effect of the stacking sequence on thermal deformation). Trans. Jpn. Soc. Mech. Eng. 2011;77:619–628.
[18] Kobayashi S, Kondo K. Danseirikigaku [Theory of elasticity]. Tokyo: Baifukan; 1987. p. 13–15.
[19] Kedward KT, Wilson RS, McLean SK. Flexure of simply curved composite shapes. Composites. 1989;20:527–536.
[20] Albert C, Fernlund G. Spring-in and warpage of angled composite laminates. Compos. Sci. Technol. 2002;62:1895–1912.
[21] Okabe Y, Yashiro S, Tsuji R, Mizutani T, Takeda N. Effect of thermal residual stress on the reflection spectrum from fiber Bragg grating sensors embedded in CFRP laminates. Compos. Part A. 2002;33:991–999.
[22] Voet E, Luyckx G, Waele W, Degrieck J. Multi-axial strain transfer from laminated CFRP composites to embedded Bragg sensor: II. Experimental validation. Smart Mater. Struct. 2010;19:105018.
[23] Luyckx G, Voet E, Waele W, Degrieck J. Multi-axial strain transfer from laminated CFRP composites to embedded Bragg sensor: I. Parametric study. Smart Mater. Struct. 2010;19:105017.